Journal of Electrochemistry

Volume 28
Issue 2 *Special Issue: Frontier of Electrochemistry (I)*

2022-02-28

Magnetic Resonance in Metal-Ion Batteries: From NMR (Nuclear Magnetic Resonance) to EPR (Electron Paramagnetic Resonance)

Bing-Wen Hu
Shanghai Key Laboratory of Magnetic Resonance, State Key Laboratory of Precision Spectroscopy, School of Physics and Electronic Science, East China Normal University, Shanghai 200241, P. R. China;,
bwhu@phy.ecnu.edu.cn

Chao Li

Fu-Shan Geng

Ming Shen

Recommended Citation

Bing-Wen Hu, Chao Li, Fu-Shan Geng, Ming Shen. Magnetic Resonance in Metal-Ion Batteries: From NMR (Nuclear Magnetic Resonance) to EPR (Electron Paramagnetic Resonance)[J]. *Journal of Electrochemistry*, 2022 , 28(2): 2108421.
DOI: 10.13208/j.electrochem.210842
Available at: https://jelectrochem.xmu.edu.cn/journal/vol28/iss2/7

【Review】 **DOI**: 10.13208/j.electrochem.210842 **Http**://electrochem.xmu.edu.cn

Magnetic Resonance in Metal-Ion Batteries: From NMR (Nuclear Magnetic Resonance) to EPR (Electron Paramagnetic Resonance)

Bing-Wen Hu*,Chao Li, Fu-Shan Geng, Ming Shen

(*Shanghai Key Laboratory of Magnetic Resonance, State Key Laboratory of Precision Spectroscopy, School of Physics and Electronic Science, East China Normal University, Shanghai 200241, P. R. China*)

Abstract: Metal-ion batteries have changed our quotidian lives. The research on the electrode materials for metal-ion battery is the key to improve the performance of the battery. Therefore, understanding the structure-performance relationship of the electrode materials can help to improve the energy density and power density of the materials. Magnetic resonance, including nuclear magnetic resonance (NMR) and electron paramagnetic resonance (EPR), has been continuously improved during the past three decades, and has gradually become one of the important technologies to study the structure-performance relationship of electrode materials. This paper summarizes the progress of magnetic resonance research from our group on several interesting electrode materials and demonstrates the important role of NMR and EPR in the study of electrode materials. This article will help to grasp the important value of magnetic resonance technology for battery research, which will promote the further development of advance magnetic resonance technology.

Key words: solid-state NMR; EPR; batteries; cathode materials

1 Introduction

Metal-ion batteries, mainly lithium-ion batteries (LIBs) and sodium-ion batteries (SIBs), have attracted a considerable attention over the past few decades because of their applications in portable electronic devices, electric vehicles, and grid storage solutions, which have a direct impact on our quotidian life[1-5]. The practical applications call for metal-ion batteries of excellent performance, i.e., higher energy density, lower cost, longer lifespan, and greater safety. To achieve good performance, the development of new electrode materials or optimization of available electrode materials that can work at high cell voltage and high specific capacity are the major important task in the field[6-11].

To develop the good electrode materials, it is important to have a fundamental understanding structure-activity relationship, that is the working mechanism and the controlling factors of the materials. Therefore, different kinds of characterization techniques (*ex-situ*, *in-situ*, *operando*) has been developed to monitor the composition and structure evolution of the electrode materials[12].

Among various characterization techniques, magnetic resonance techniques, including nuclear magnetic resonance (NMR, including magnetic resonance imaging (MRI)) and electron paramagnetic resonance (EPR, including electron paramagnetic resonance imaging (EPRI)) are unique tools to probe structural information and phase information at atomic-level and to measure ionic motion at various time-scales.

Solid-state NMR spectroscopy (ssNMR) can pro-

Cite as: Hu B W, Li C, Geng F S, Shen M. Magnetic resonance in metal-ion batteries: From NMR (nuclear magnetic resonance) to EPR (electron paramagnetic resonance). *J. Electrochem.*, 2022, 28(2): 2108421.

Received: 2021-08-21, Revised: 2021-09-08. *Corresponding author, Tel: (86-21)62233633, E-mail: bwhu@phy.ecnu.edu.cn

vide a wealth of information on the materials in a non-disruptive and non-invasive manner, and is suitable for characterizing common light elements in electrode materials such as $^{6/7}$Li, ^{23}Na, ^{31}P, ^{19}F, ^{1}H, ^{13}C, etc., especially ^{17}O, which provides a powerful tool for studying atom environmental changes and valence processes[13]. For different types of observable atomic nuclei, suitable advance ssNMR methods (e.g., pjMATPASS: projected magic-angle-turning phase-adjusted-sideband-separation, Hahn-echo, HMQC: heteronuclear multiple quantum coherence) can be deliberately selected to analyze the evolution of the short-range structure and electronic structure of battery materials. EPR, which is adept in studying metal ions (e.g., V, Co, Ni, Mn, Fe) containing unpaired electrons on the atomic orbital with high sensitivity, can help to characterize the electronic state and coordination state, and then elucidate the redox evolution of the metal center[14]. ssNMR and EPR are two complementary techniques.

MRI and EPRI can provide chemical environment information at different spatial locations[15,16]. MRI could be used to study the metal anodes and different kinds of electrolytes targeting at the specific nuclei ($^{6/7}$Li and ^{23}Na). However, the 2D (two-dimension) or 3D (three-dimension) MRI often has low spatial resolution (~ mm) due to the use of low-power gradients. To improve the spatial resolution, MRI is often performed in the 1D mode, using high-power *Z*-axis gradient. However, in the 1D mode, NMRI could detect the growth of the Li- dendrite in side view, but could not catch the Li growth in front view. To improve the spatial resolution, EPRI could be employed to monitor the metal anodes with the relatively high resolution of ca. 50 ~ 100 μm per pixel.

In this review, we focus on the topic of the electrode materials studied by NMR and EPR in our group. For solid polymer electrolytes, readers could refer to another review of our group on this topic. In the following part, the application of NMR will be discussed first, followed by the application of EPR, and finally, the combined use of NMR and EPR will be discussed.

2 Typical NMR Studies

2.1 ^{17}O and ^{59}Co NMR Studies of $LiCoO_2$

To the best of our knowledge, previous NMR studies of $LiCoO_2$ have focused on ^{6}Li, ^{7}Li and ^{59}Co species, no ^{17}O NMR studies have reported to probe the oxygen atoms in $LiCoO_2$. Our group has successfully produced the ^{17}O-labeled $LiCoO_2$ and obtained the ^{17}O NMR spectra to investigate the structural evolution of Li_xCoO_2 ($0 \leqslant x \leqslant 1$) during delithiation processes (Figure 1)[17]. Here x denotes the mole fraction of Li^+ in Li_xCoO_2.

From $0.85 \leqslant x \leqslant 1.0$, only one peak at -636 ppm with the roughly the same intensity could be observed. This peak belongs to O3I insulator phase with low conductivity, which is a kind of O3H (O3 with hexagonal structure) phase. From $0.75 \leqslant x \leqslant 0.5$, the peak at -636 ppm decreased quickly, suggesting that a large amount of paramagnetic Co^{4+} makes the ^{17}O signal unobservable. This phase belongs to O3II conductor phase with high conductivity, which is also a kind of O3H phase. Due to the same chemical shift, O3I and O3II should have the very similar crystal structure. However due to the extraction of Li-ions, the c axis might be different, leading to different XRD diffractions for O3I and O3II phases.

At $x = 0.5$, a new set of peaks at 900 ppm began to appear. The results by fitting this set of peaks showed two peaks with similar C_Q (quadrupolar coupling constant). These two peaks could be assigned to the monoclinic $Li_{0.5}CoO_2$ phase, indicating the occurrence of a hexagonal-monoclinic phase transition (O3H → O3M). Here, it should be pointed out that $Li_{0.5}CoO_2$ is proposed for this intermediate phase at $x = 0.5$, while the previous ^{7}Li NMR suggested an intermediate phase of $Li_{0.75}CoO_2$. The phase at $0.15 \leqslant x \leqslant 0.45$ has been assigned to O3III phase, however, this phase should have the very similar structure to O3M phase at $x = 0.5$, as suggested by NMR results. This set of two peaks disappeared at $x = 0.18$, and then a new peak at 1250 ppm was observed. The peak at 1250 ppm can be assigned to the H1-3 phase.

Accordingly, the ^{59}Co spectra have also been acquired. The ^{59}Co NMR spectra had only one peak that

only existed when $x \geqslant 0.5$. It is suggested here that a large amount of Co^{4+} generated after $x < 0.5$, and then the electrons would hop between two Co^{4+} ions with $t_{2g}^5e_{2g}^0$ configuration through t_{2g}-t_{2g} overlap, resulting in electron delocalization, which makes the ^{59}Co NMR signal unobservable.

The C_Q value (~ 7 MHz) for the monoclinic phase obtained the ^{17}O NMR results is quite large, indicating that there is very strong covalent bonding between Co and O atoms. Therefore, when charging at high-voltage, the Co-O bond is difficult to be distorted due to the directionality of the strong covalent bond, and the hexagonal-to-monoclinic phase transition takes place instead of local structural distortion. Thus, the charge of $LiCoO_2$ higher than 4.2 V with $x < 0.5$ will lead to the structural instability.

2.2 *In-Situ* NMR Study of $LiCoO_2$

In recent years, *in-situ* NMR technology for the real-time analysis of the battery has been well developed. Most *in-situ* NMR studies were performed with a plastic cell in the static mode without magic angle spinning, and static NMR spectra show very broad line-shapes, which is difficult to be analyzed. Recently, a novel jelly-roll cell design was proposed for *in-situ* NMR and MAS (magic angle spinning) NMR spectra could be acquired for high resolution of the peaks[18]. However, when the NMR data acquisition started, the wires had to be removed. During the detachment time of the wires, the system state would relax back to the equilibrium state. Subsequently, the wires were reattached for the following charging or discharging process.

Shimoda et al. conducted *in-situ* NMR studies on the charge and discharge processes for Li||$LiCoO_2$ with plastic cell[19]. Our group also employed *in-situ* ^7Li NMR to study uncoated and Ba-Ti-coated (barium

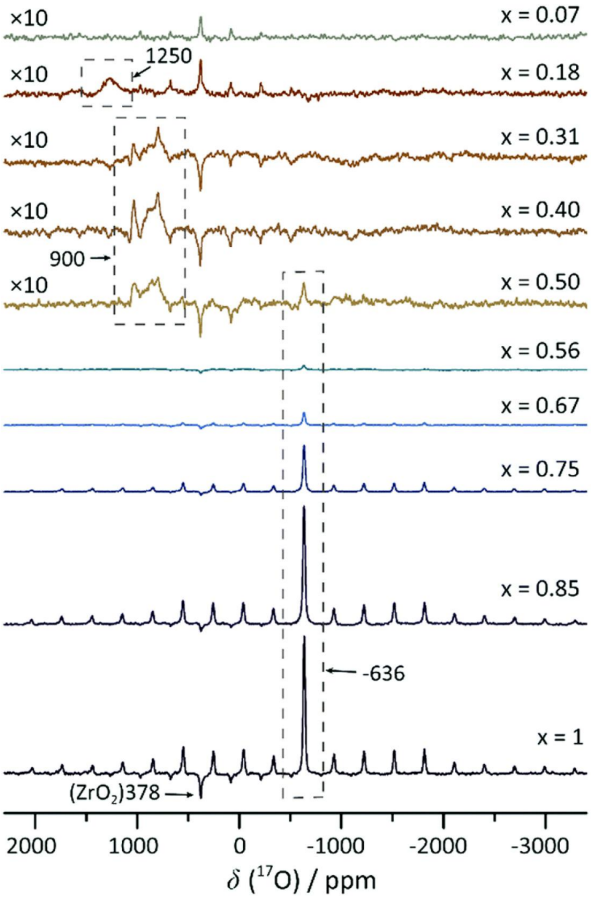

Figure 1. *Ex-situ* ^{17}O MAS NMR spectra of Li_xCoO_2 recorded at 14.1 T and 24 kHz MAS. The magnification factors are listed on the left side of each spectrum. (Reproduced from Ref.[17] with permission from The Royal Society of Chemistry) (color on line)

and titanium coated) $LiCoO_2$ samples with plastic cell[20]. The pristine $LiCoO_2$ is in the O3I phase with insulator character. *In-situ* NMR results suggested that the uncoated $LiCoO_2$ sample could not return to the pristine state after being charged to a high voltage of 4.5 V and then discharged to 3.0 V. The final state of uncoated $LiCoO_2$ after charge/discharge process had O3I-O3II coexisted, that is, the conductor phase and the insulator phase coexisted. This result is identical to the result of Shimoda[19]. The Ba-Ti-coated $LiCoO_2$ samples could return to the pristine O3I phase through O3II-O3I phase transition upon the same charge/discharge process, because this sample had higher electrical conductivity due to the formation of TiO_2 layer and $BaTiO_3$ particles on the surface after the Ba-Ti coating. Therefore, it could be anticipated that the Ba-Ti coating can greatly improve the electrical conductivity and make the conductor-insulator phase transition more reversible.

3 Typical EPR Studies

3.1 *In-Situ* EPR Study of $NaCrO_2$

$NaCrO_2$ is a candidate cathode material for sodium-ion batteries due to its safety, low cost, and high-power density. To increase the energy density, it is important to extract more Na ions at higher voltage, however, this often leads to fast capacity decay and irreversible structural transformation to CrO on the surface.

In-situ EPR was carried out to monitor the evolution of $NaCrO_2$ cycled between 2.2 ~ 3.6 V and 2.2 ~ 4.5 V[21]. The electrochemical process was reversible for the cutoff voltages of 3.6 V (Figure 2(B)), whereas the discharge capacities decreased fast as the cutoff voltage rises to 4.5 V (Figure 2(D)). As shown in Figure 2(A), the *in-situ* EPR spectra for the first two cycles with an upper cutoff voltage of 3.6 V clearly reveals the good reversibility during the charge/discharge processes. It should be pointed out here that the EPR intensity at $g = 1.962$ decreased and vanished within 3 h (ca. 0.12 Na removed) when it starts charging (Figure 2(B)). The loss of the EPR signal, is possibly originated from the electronic de localization within the [CrO_2] layers due to the overlap between the adjacent Cr t_{2g} orbitals. An increase of the EPR intensity after ca. 18 h was observed when fully discharged, implying the relocalization of the electrons and the Cr reduction to +3. The *in-situ* EPR spectra cycled between 2.2 and 4.5 V are shown in Figure 2(C). It could be observed that the signal at $g = 1.962$ was not recovered in the discharge process after charging to 4.5 V. An unexpected new signal was observed with $g = 1.977$ at the beginning of the voltage plateau with respect to the irreversible phase transition (Figure 2 (D)).

EPR imaging (EPRI) was carried out on the *in-situ* cell in order to determine its spatial distribution of this unknown signal. It could be observed in Figure 3 that this signal was distributed in an area of 8 × 4 mm and a thickness of 1.5 mm, consistent with the size of the separator used in the cell. Therefore, this unknown species associated with the irreversible phase transition should be located in the electrolyte, which is then attributed to the Cr^{5+} ions dissolved with the surface reconstruction. This is the first report on the presence of soluble Cr^{5+} species from Cr-based cathode material. A disproportionation-dissolution mechanism is suggested here that the Cr disproportionation on the surface could take place as $Cr^{3+} + Cr^{4+} \leftrightarrow Cr^{2+} + Cr^{5+}$ and then dissolution of Cr^{5+} into the electrolyte would lead to a densified rock-salt CrO as the reaction proceeds to the right side.

3.2 EPR Study of $Li_3V_2(PO_4)_3$

Ex-situ X-band EPR was employed to study lithiation/delithiation process of monocline $Li_3V_2(PO_4)_3$ calcinated from vanadium metal-organic framework precursor MIL-101(V)[22]. All the EPR spectra were collected at the temperature of 2 K, as shown in Figure 4. In the perpendicular mode, $V^{4+}(t_{2g}^1e_g^0, S = 1/2)$ is often observable while $V^{3+}(t_{2g}^2e_g^0, S = 1)$ is "EPR-silent" with no observable signal because its zero-field splitting in $S = 1$ ground state is usually larger than the available microwave quantum. $V^{5+}(t_{2g}^0e_g^0, S = 0)$ has no EPR signal with $3d^0$ configuration.

The pristine sample and the sample at 3.63 V showed a narrow signal at $g \sim 2.00$ corresponding to free electrons from the super-P conducting additives.

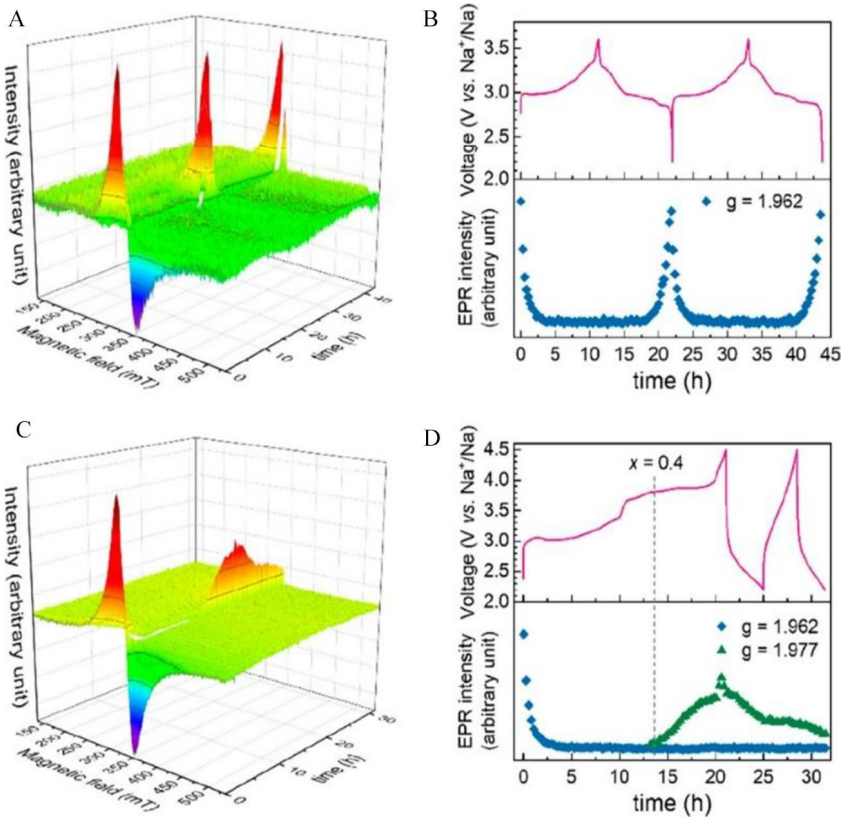

Figure 2. *In-situ* EPR spectra of the $NaCrO_2$/Na cell cycled at 10 mA·g^{-1} between (A) 2.2 ~ 3.6 V and (C) 2.2 ~ 4.5 V. The intensive Na signal in the range of 331 ~ 335 mT is truncated for clarity. (B, D) Corresponding voltage profiles (top) and EPR intensities (bottom) as a function of time. EPR intensities are calculated using half of the peak-to-peak intensity. (Reproduced from Ref.[21] with permission from American Chemical Society) (color on line)

When the sample was charged to 3.72 V or discharged to 3.56 V, a new peak could be observed at ~ 200 G, which arised from a new spin state S = 3/2 due to the ferromagnetic coupling between V^{3+} and V^{4+}. Therefore, this peak at ~ 200 G suggests the existence of V^{4+} at this voltage. This ferromagnetic coupling also confirmed the existence of V^{3+}/V^{4+} ordering for $Li_2V_2(PO_4)_3$ at the charging voltage of 3.72 V. Although V^{3+}/V^{4+} ordering had been suggested by NMR result at ca. 3.72 V[23], the EPR result is a stronger proof of V^{3+}/V^{4+} ordering.

After charging to 4.12 V, the peak at ~ 200 G disappeared and a new peak at ~ 3426 G ($g_{eff} \approx 1.96$) could be observed, suggesting that most of V^{3+} ions have been transformed to V^{4+} ions, which cancelled the ferromagnetic coupling and hence the peak at ~ 200 G vanished. Further charging to 4.60 V led to the reduction of V^{4+} signal, because V^{4+} was oxidized to V^{5+} which has no EPR signal. The EPR spectra of discharge process show a typical reversible feature with respect to the charge process, demonstrating the good reversibility of this $Li_3V_2(PO_4)_3$ sample during the charge/discharge processes. Using EPR technique, the valence states of V-ion were explicitly revealed; especially, the ferromagnetic coupling could be revealed.

3.3 EPR Study of Coordination Polymer Anode

Coordination polymers (CPs) or metal-organic frameworks (MOFs) constructed by metal ion nodes and bridging ligands, are emerging as a novel class of energy storage materials for rechargeable batteries. The electrochemical process of cobalt nitrilotriacetic acid CP nanorods (r-CoHNta) was analyzed by continuous-wave (CW) X-band EPR spectra recorded at 2 K, as shown in Figure 5[24].

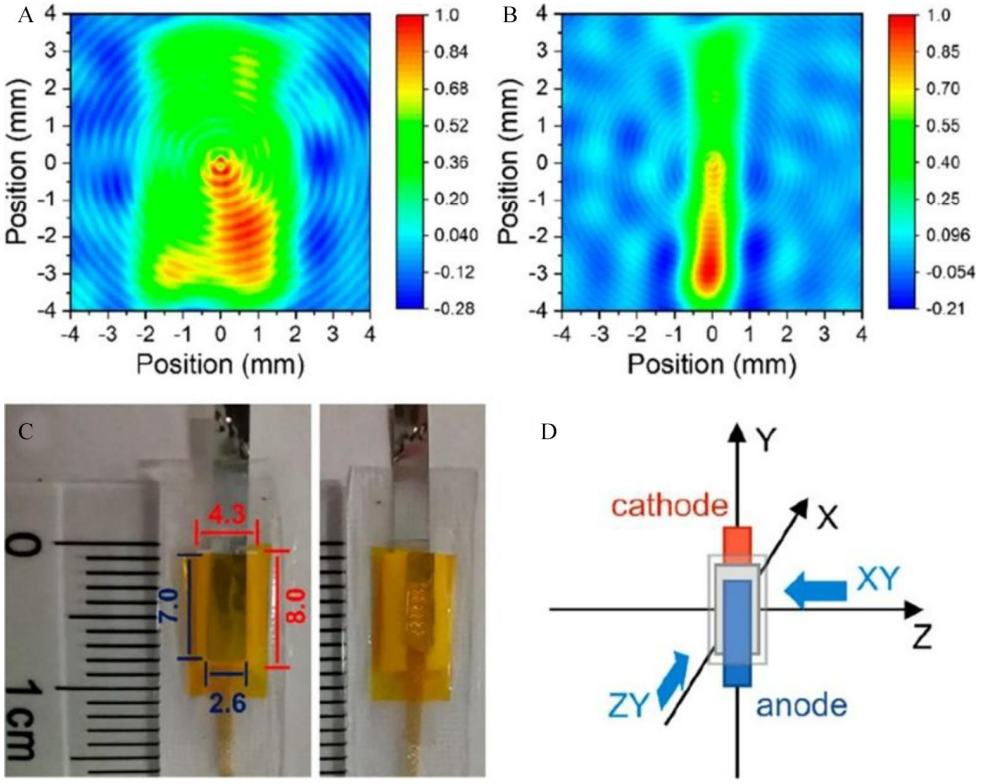

Figure 3. *In-situ* EPR images of the *in-situ* cell charged to 4.15 V on (A) the ZY plane and (B) the XY plane. Color bars on the right side show the normalized intensity of spin concentrations. (C) Digital photos of the cell used in EPR imaging. The sizes of the cathode and the separator are marked in blue and red, respectively. (D) Scheme for the orientation of the cell in the image coordinates. (Reproduced from Ref.[21] with permission from American Chemical Society) (color on line)

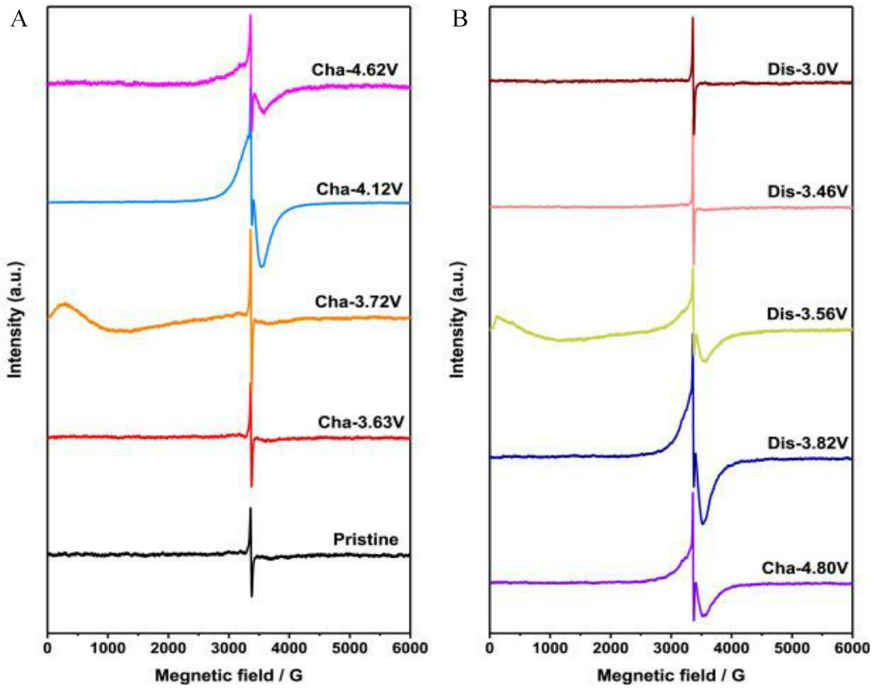

Figure 4. (A, B) *Ex-situ* X-band EPR spectra of $Li_3V_2(PO_4)_3$ electrode materials cycled at different states-of-charge at 2 K. Cha denotes "charging" and Dis denotes "discharging". (Reproduced from Ref.[22] with permission from Elsevier publisher) (color on line)

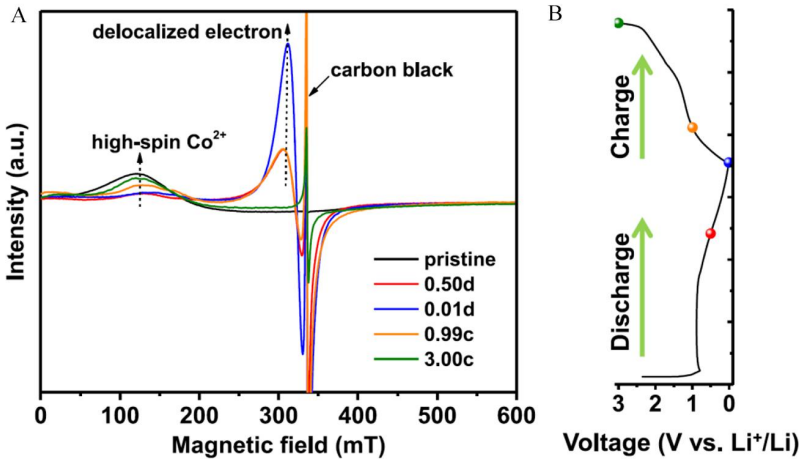

Figure 5. (A) X-band EPR spectra for lithiation/delithiation of the r-CoHNta electrode materials cycled to different states-of-charge recorded at 2 K; (B) The corresponding electrochemical profile cycled at a current rate of 100 mA·g^{-1}. (Reproduced from Ref.[24] with permission from Elsevier publisher) (color on line)

The intense sharp signal ($g \approx 2.00$ at 340 mT) can be attributed to the free electron from super-P conductive additives. The EPR spectrum of the pristine r-CoHNta was dominated by a broad derivative lineshape with peak intensity around $g \sim 4.3$ at 130 mT, which is characteristic of rhombic high-spin ($S = 3/2$) Co^{2+} ($t_{2g}^5e_g^2$), disclosing that the Co-ions in pristine r-CoHNta are weak 6-coordination. The most interesting result is that Li-ion insertion into r-CoHNta (the curve of 0.01d in Figure 5(A)) led to a Dysonian-lineshape EPR absorption around ~ 312 mT ($g \sim 2.07$). It is well established that the Dysonian lineshape of EPR signal is the feature of delocalized conducting electron. The delocalized conducting electron might come from delocalized high-spin Co^{2+} or from Co-metal clusters. Therefore, this result suggests that the high spin Co^{2+} releases some electron spins from the localized electrons after Li^+ intercalation. Several MOF anodes were also investigated by EPR techniques[25-27].

4 Combination of NMR and EPR for Research

4.1 Study of $Na_3V_2(PO_4)_2F_{3-2y}O_{2y}$ or $Na_3V_2(PO_4)_3$

Our group has studied the series samples of $Na_3V_2(PO_4)_2F_{3-2y}O_{2y}$ (y = 1.0, 0.8, and 0.6), produced by a microwave-assisted solvothermal procedure[28, 29]. The three samples were called as NVOPF, $NV_{3.8}$OPF and $NV_{3.6}$OPF, among which the average valence states of V-ion are +4, +3.8 and +3.6, respectively. The NVOPF had only one ^{23}Na peak at 91.5 ppm (Figure 6(A)), suggesting that the synthesis method could eliminate, to a great extent, the defects, which was observed previously by Park et al[30]. For $NV_{3.8}$OPF, two major peaks at 89.4 and 128.7 ppm were observed, which comes from Na^+ close to V^{4+} and V^{3+} ions, respectively, considering that paramagnetic hyperfine interaction of V^{3+} to Na is stronger compared to V^{4+} ions. The ^{23}Na MAS NMR spectrum of $NV_{3.6}$OPF was broader, implying the stronger paramagnetic environment due to more V^{3+} ions generated. The ^{31}P NMR spectra also demonstrated the broadening effect of the V^{3+} ions (Figure 6(B)).

Continuous-wave (CW) X-band EPR spectra were recorded under 2 K to further interpret the valence state of V-ions. The NVOPF exhibited a featureless first-differential spectrum centered at g-value of 1.93 with ~ 100 G peak-to-trough (Figure 6(C)). This g-value was close to that of free electron ($g_e = 2.0023$), suggesting the existence of V^{4+} with electron configuration $t^1_{2g}e^0_g$ ($S = 1/2$). However, the EPR signal intensities of $NV_{3.8}$OPF and $NV_{3.6}$OPF were much weaker than that of NVOPF (namely, NVOPF > $NV_{3.8}$OPF > $NV_{3.6}$OPF), indicating a lower content of V^{4+} centers

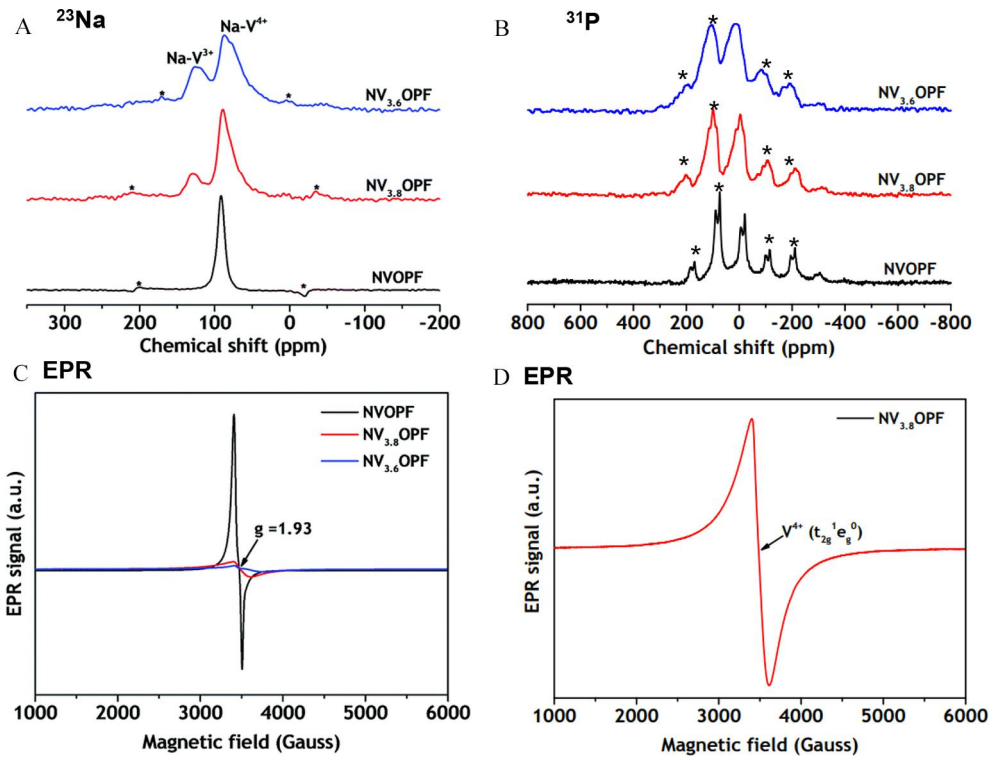

Figure 6. (A) ^{23}Na and (B) ^{31}P MAS ssNMR spectra of NVOPF, $NV_{3.8}OPF$, and $NV_{3.6}OPF$. Spinning sidebands are marked with asterisks in (A) and (B). (C) Continuous-wave X-band EPR spectra recorded at 2 K of NVOPF, $NV_{3.8}OPF$, and $NV_{3.6}OPF$. (D) An enlarged EPR spectrum of $NV_{3.8}OPF$. (Reproduced with permission from ref.[28], Copyright 2018, The Royal Society of Chemistry) (color on line)

in these systems. Here the signal observed only came from V^{4+}, since V^{3+} ($t^2_{2g}e^0_g$, $S = 1$) is "EPR-silent" as it is a non-Kramer's ion with integral J in LS coupling. In addition, the EPR peak of $NV_{3.8}OPF$ was much broader than that of NVOPF (Figure 6(D)), suggesting the presence of V^{3+} centers that significantly broaden the peak of V^{4+} due to strong electron dipole-dipole couplings between V^{3+} and V^{4+}.

In-situ ^{23}Na NMR spectra of Na/$NV_{3.8}POF$ cell cycled at a current rate of 0.05C during the first charge and discharge processes were first acquired. Due to the low resolution the *in-situ* static NMR spectra, ^{23}Na MAS spectra were then acquired[29]. For the pristine $NV_{3.8}OPF$ ($Na_3V_2(PO_4)_2F_{1.4}O_{1.6}$) sample, only Na^+ signals close to V^{3+} and V^{4+} were observed at ~ 130 and ~ 90 ppm. After the extraction of two Na ions from $Na_3V_2(PO_4)_2F_{1.4}O_{1.6}$, $Na_1V_2(PO_4)_2F_{1.4}O_{1.6}$ with average covalence state of 4.8 was produced, having two Na peaks neighboring to V^{4+} and V^{5+} at ~ 90 and ~ 6.5 ppm, respectively. To confirm V^{5+} ion being existed in this system, the ^{51}V MAS ssNMR spectrum of $Na_1V_2(PO_4)_2F_{1.4}O_{1.6}$ was acquired, having an obvious signal located in the region of [-550, -720] ppm.

The ^{23}Na MAS ssNMR spectra for the charge process of $NV_{3.8}POF$ (Figure 7(A)) could be grouped into two different stages (I and II): In Stage I, the main peak at ~ 90 ppm showed a continuous shift to lower frequencies, and this symmetric lineshape became asymmetric with apparent shoulder peaks at the right side. In Stage II, this main peak showed an shift back to higher frequency. Such a phenomenon was not observed in the NV_4POF system. The NMR result of $NV_{3.8}POF$ in the early stage II is counterintuitive, because it was believed that upon Na extraction, V^{3+} should be converted to V^{4+} and V^{4+} should be converted to V^{5+}, leading to an overall shift to lower frequency. This observation could be explained by EPR measurements. Parallel-mode EPR revealed two dispersion peaks at $g = 4.01$ and $g = 1.93$ (Figure 7(B))[29]. The signal at $g = 4.01$ indicates the transition be-

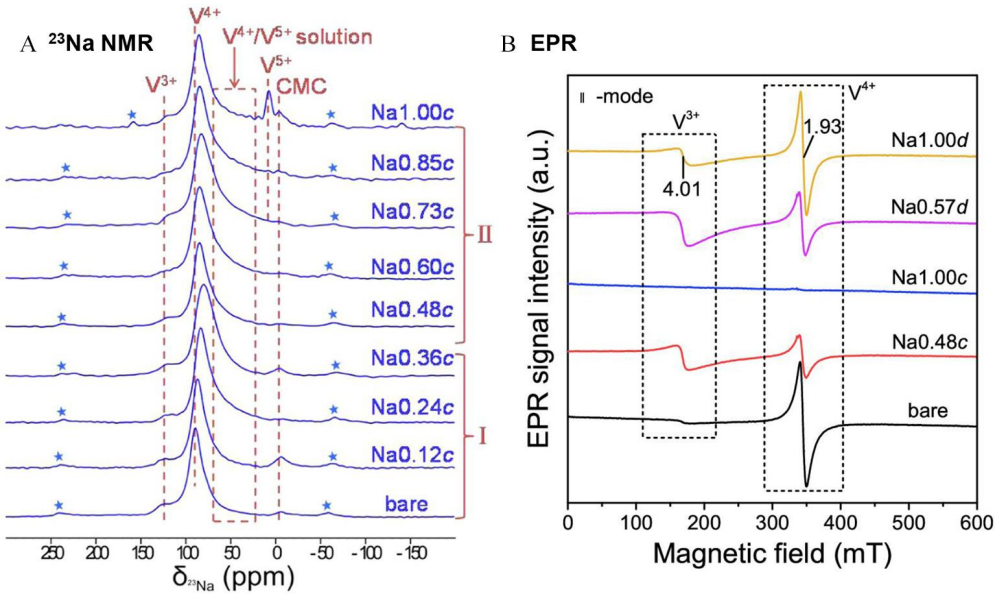

Figure 7. (A) ^{23}Na MAS ssNMR spectra of the $NV_{3.8}POF$ electrodes under various SOC (states-of-charge) values during charge process; (B) Parallel-mode EPR spectra of cycled $NV_{3.8}POF$ under representative SOC. (Reprinted with permission from ref.[29], Copyright 2018, American Chemical Society) (color on line)

tween |+1> and |-1> doublet of an S = 1 spin state, which can be ascribed to V^{3+} with $t^2_{2g}e^0_g$ configuration. It should be mentioned that S = 1 configuration could not be observed with perpendicular-mode EPR. The increase of the V^{3+} content in $Na_2V_2(PO_4)_2F_{1.4}O_{1.6}$ (Na0.48c, $V^{4.3+}$ covalence state) was obtained as compared with that in bare $Na_3V_2(PO_4)_2F_{1.4}O_{1.6}$, which inferred that during the Na-ion extraction, the charge disproportionation of two V^{4+} to a mixture of V^{3+} and V^{5+} possibly occurred in the stage II, which leads to abnormal phenomenon in the ^{23}Na NMR spectra in Stage II. In the charged NV_4POF sample, that is, $Na_2V_2(PO_4)_2F_1O_2$, no charge disproportionation was observed and no generated V^{3+} as suggested by the NMR spectra.

Another skin system boron-doped $Na_3V_2(PO_4)_3$ had also been studied by NMR and EPR with similar techniques[31]. EPR results under 1.8 K confirmed the generation of V^{2+} with rhombohedral distortion upon the fourth Na^+ intercalation process of $Na_3V_2(PO_4)_3$ at low voltage of ~ 1.6 V, which is further confirmed by ^{23}Na ssNMR experiments. The results from NMR and EPR suggested that the boron substitution can widen the range of solid-solution reaction, facilitate the structural transformation toward V^{2+}-containing phase, and mitigate the short scale heterogeneity of P and Na nuclei[31].

4.2 Study of $Na_xLi_yMn_{1-y}O_2$ Cathodes

Two cathode materials, $Na_{0.72}Li_{0.24}Mn_{0.76}O_2$ (NLMO) and $Na_{0.72}Li_{0.24}Mn_{0.66}Ti_{0.1}O_2$ (NLMTO-0.1) were studied by NMR and EPR[32]. Cyclic charge/discharge studies show that the stability of Ti-doped NLMTO-0.1 far exceeded NLMO. The ^{7}Li pj-MATPASS ssNMR spectra (Figure 8) were used to probe the structural evolution. For pristine NLMO (Figure 8(C)), the typical resonance observed at ~ 746 ppm can be attributed to Li ions in the Na layer, whereas the resonances centered at ~ 1490 and ~ 1850 ppm can be assigned to Li sites in a honeycomb-like arrangement within the TMO_2 layer. In particular, after Ti-doping, most of the peaks for NLMO-0.1 had been largely broadened (Figure 8 (A)), due to more distorted coordination environments. Figure 8(B) shows that when Ti-doped NLMTO-0.1 was charged to 4.5 V and then discharged to 1.5 V, Li would return to the MnO_2 layer (the yellow region in Figure 8). However, when the NLMO sample went through the same process, Li would prefer to stay in the Na layer (the blue region in Figure 8). It

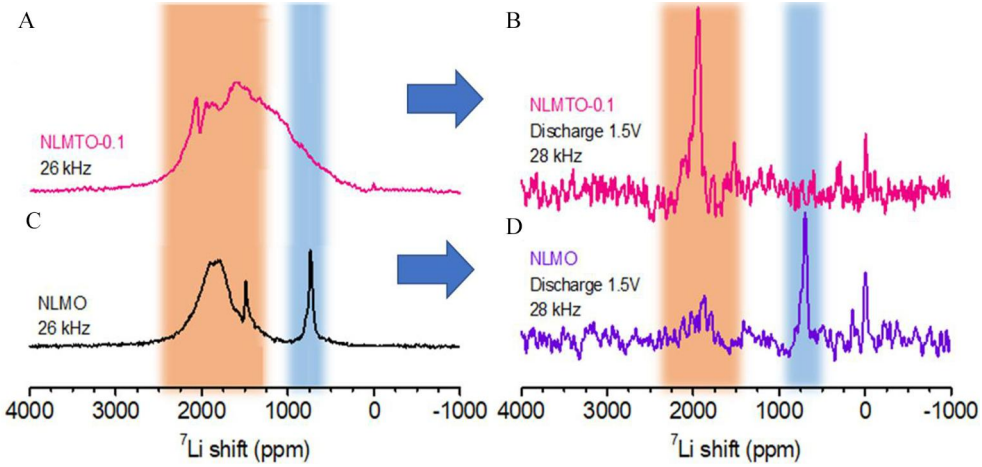

Figure 8. Isotropic slices of ^{7}Li pj-MATPASS NMR spectra for (A, C) pristine NLMO, and NLMTO-0.1, and (B, D) fully discharged NLMO and NLMTO-0.1 electrodes. The resonances within the blue-marked region correspond to the Li sites in the Na layer, while the resonances within the yellow-marked region correspond to the Li sites within the TMO_2 layer. (Reproduced from Ref.[32] with permission from American Chemical Society) (color on line)

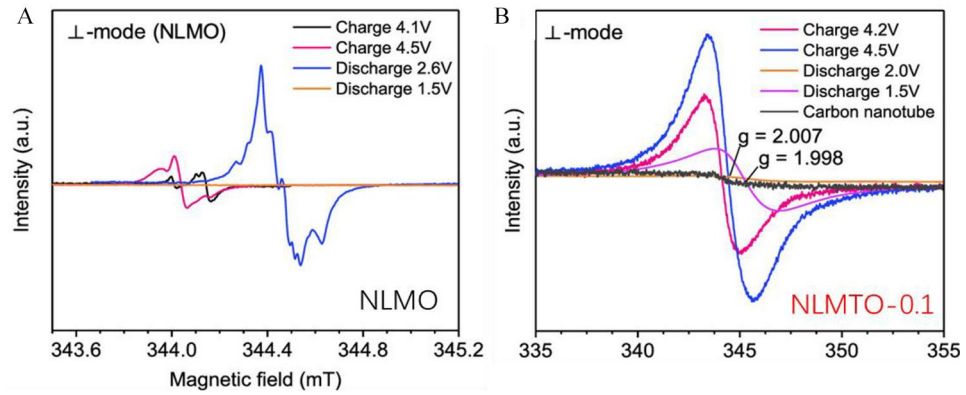

Figure 9. (A) Fine scanning vertical-mode EPR spectra of cycled NLMO under the representative SoC; The O_2^{n-} EPR signals possess various hyperfine patterns. (B) Fine scanning vertical-mode EPR spectra of cycled NLMTO-0.1. (Reproduced from Ref.[32] with permission from American Chemical Society) (color on line)

should be pointed out here that the Li staying in the Na layer will lead to a large number of vacancies in the MnO_2 layer. The existence of vacancies makes Mn tend to move and cause its structural instability.

The EPR experiments (Figure 9) showed that in these two systems, the O_2^{n-} signal with an effective *g*-value of 2.007 would appear after charging to 4.2 V, but the signal evolution of NLMTO-0.1 became more reversible. Especially, the EPR signal of NLMTO moved along the *x*-axis upon charging and discharging, while that of NLMTO-0.1 stayed at the similar position, further showing the better reversibility of oxygen redox reaction in the NLMTO-0.1 system. The combined use of NMR and EPR shows that Ti doping can make Li return to the MnO_2 layer, and then make the oxygen reaction more reversible, thereby increasing the stability of the cathode materials.

Similar techniques were also applied to Sn/Zr-substituted P2-$Na_{0.66}Li_{0.22}Mn_{0.78}O_2$ system[33]. The ^{23}Na ssNMR spectra shows that when charged to 4.5 V, the ^{23}Na signal would be changed from a sharp peak at ~ 1708 ppm to a broad peak ranging from 1560 to -300 ppm, signifying a considerable disordering around the residual Na ions, which further confirms the gen-

eration of stacking faults at high voltage of 4.5 V that disrupt the long-range order. The ^{7}Li ssNMR after long 50 cycles at low voltage of 1.5 V suggested the gradual loss of the ^{7}Li in the MnO_2 layer. EPR also showed the existence of O_2^{n-} signal. NMR and EPR results validate that (i) Li migrates from TM layer to AM layer upon charge, and do not fully return to the original sites in TM layer upon discharge; (ii) the extraction/insertion of Na leads to the local structural transition which is not fully reversible; (iii) Li/Mn migrations keep going, leading to irreversible Li/Mn losses and Na-site local disorder upon prolonged cycling.

4.3 Study of Cation-Disordered Rock-Salt $Li_{1.2}Ti_{0.4}Mn_{0.4}O_2$ Cathode Material

We also used EPR and NMR to study the changes in the local atomic environment and electronic structure of the cation-disordered cathode material $Li_{12}Ti_{04}Mn_{0.4}O_2$ during the first cycle of charge and discharge[34]. It was found by ^{7}Li ssNMR that Li ions were preferentially extracted from the Li-rich environment, which forms 0-TM percolation channel. However, the irreversible loss of Li in the diamagnetic environment after one cycle was observed in ^{7}Li NMR, indicating that the 0-TM channel was partially destroyed. The ^{17}O NMR reveals that an anomaly occurred in both ^{7}Li and ^{17}O shifts at the end of charging to 4.8 V, since a decrease of the ^{17}O peak shift and a steep rise in the ^{7}Li weighted average shift were observed. Such an anomaly implies the oxygen redox reactions.

The EPR spectrum (Figure 10) of pristine $Li_{1.2}Ti_{0.4}Mn_{0.4}O_2$ had no signal, however, upon charging, a

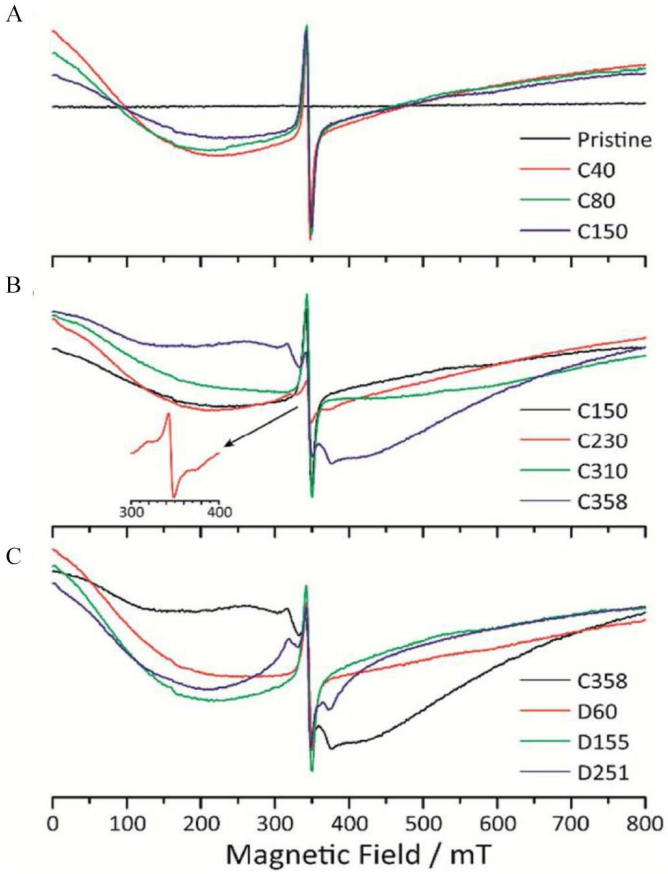

Figure 10. *Ex-situ* perpendicular-mode CW-EPR spectra of LTMO during the processes of (A) Mn oxidation, (B) O oxidation, and (C) reduction. These EPR measurements were performed at 1.8 K. Signal intensities are normalized based on the mass of each material scraped from the electrodes. The sharp signals centered at ~ 345 mT (g ~ 2.0) stem from the delocalized electrons in the conductive carbon black, which can be regarded as an external reference although it may cover up similar signals. (Reproduced from Ref.[34] with permission from The Royal Society of Chemistry) (color on line)

prominent broad line resonating at ca. 90 mT ($g \sim 7.5$) was observed, which arises from the ferromagnetic resonance. This result suggests the presence of short-range ferromagnetism due to the local clusters of Mn ions. At the beginning of oxygen oxidation (C230, ~ 4.3 V), a new weak EPR signal appearing at $g \sim 2.0$ is assigned to $(O_2)^{n-}$ species. However, this $(O_2)^{n-}$ signal disappeared for C310 (~ 4.5 V) as oxidation proceeded. When charging to a high voltage of 4.8 V (C358), a signal analogous to that of the $(O_2)^{n-}$ species appeared with stronger intensity, which should be ascribed to the localized electron holes on the lone-pair states of O whose other 2p orbitals are bonded to Mn. Furthermore, the results of Fast Fourier transforms (FFTs) of the TEM images suggested that short-range order (SRO) occurs when charging begins and the TM cation migration takes place during O oxidation to relax the distorted lattices, resulting in a local disorder-to-order transition, which deteriorates the diffusion kinetics of Li ions.

The combined use of NMR and EPR confirmed the migration and the aggregation of Mn ions, together with the change of 0-TM environment and oxygen environment during charge and discharge, which leads to an undesirable voltage hysteresis and low coulombic efficiency.

5 Conclusions

To conclude, ssNMR/EPR is a powerful tool to investigate electrode materials. NMR could probe the environment evolution of different kinds of nuclei with high-resolution, such as ^{7}Li, ^{23}Na, ^{19}F, ^{17}O and especially ^{59}Co, providing direct evidence for structural evolution together with the subtle information of phase transition. EPR could probe different kinds of metal ions (e.g., V, Co, Ni, Mn, Fe) containing unpaired electrons and several metal electrodes (e.g., Li, Na) with high sensitivity. It could be employed to characterize the electronic state and the redox state of metal ions. Table 1 summarizes different NMR/EPR techniques and their applications. The explicit physical background could be found in the ref.[35]. It should be pointed out here that as the electrode material system becomes more and more complex, the advance NMR/EPR techniques, together with DFT (Density Functional Theory) calculations are urgently needed. Our group has used VASP and Quantum Espresso (QE) software together to calculate ^{17}O NMR and EPR parameters (e.g., g-value), laying a foundation for the explanation of NMR and EPR signals[36]. Readers could read DFT-related literatures for details[37-41]. The re-

Table 1 Summary of important magnetic resonance techniques and their applications

Technique	Application
MQMAS (multiple-quantum magic angle spinning)	Obtain high-resolution 2D NMR spectra of half-integer quadrupolar nuclei, e.g., ^{23}Na($Na_3V_2(PO_4)_2F_{3-2y}O_{2y}$), ^{17}O.
pjMATPASS (projected magic-angle-turning phase-adjusted-sideband-separation)	Obtain high-resolution NMR spectra with large chemical-shift-anisotropy broadening due to hyperfine interactions, e.g., ^{7}Li($Na_{0.72}Li_{0.24}Mn_{0.76}O_2$), ^{31}P, ^{19}F($Na_3V_2(PO_4)_2F_{3-2y}O_{2y}$).
WURST-CPMG(wideband uniform rate smooth truncation Carr-Purcell Meiboom-Gil)	Obtain static broad NMR spectra, e.g., ^{14}N, ^{95}Mo (MoS_2).
2D homonuclear correlation and exchange (2D EXSY)	Study dynamic or chemical exchange processes, e.g., ^{7}Li and ^{23}Na.
2D homonuclear correlation based on dipole coupling (i.e. RFDR)	Detect neighboring atoms in space to reveal the spatial proximity, e.g., ^{1}H, ^{7}Li, and ^{31}P.
Perpendicular mode EPR	Detect the transitions between eigenstates for systems with half-integer spin, e.g., V^{4+}.
Parallel mode EPR	Detect the transitions between eigenstates for systems with integer spin, e.g., V^{3+}.

sults from the combination of NMR and EPR have important implications for the interpretation of the working mechanism and structure-activity relationship.

Above all, these investigations might pave the way towards better understanding of the structural evolution mechanism and the design of the stable high-capacity electrode materials in the future. More application using NMR and EPR techniques to electrode materials is expecting.

Acknowledgements:

Authors are grateful for the funding supported by National Natural Science Foundation of China (No. 21872055, No. 21874045), Shanghai Science and Technology Innovation Action Plan (No. 19142202900) and Fundamental Research Funds for Central Universities and Open Foundation of ECNU (No. 42125102).

References:

[1] Vaalma C, Buchholz D, Weil M, Passerini S. A cost and resource analysis of sodium-ion batteries[J]. Nat. Rev. Mater., 2018, 3(4): 18013.

[2] Hwang J Y, Myung S T, Sun Y K. Sodium-ion batteries: present and future[J]. Chem. Soc. Rev., 2017, 46(12): 3529-3614.

[3] Fang C, Huang Y H, Zhang W X, Han J T, Deng Z, Cao Y L, Yang H X. Routes to high energy cathodes of sodium-ion batteries[J]. Adv. Energy Mater., 2016, 6(5): 1501727.

[4] Choi J W, Aurbach D. Promise and reality of post-lithium-ion batteries with high energy densities[J]. Nat. Rev. Mater., 2016, 1(4): 16013.

[5] Yabuuchi N, Kubota K, Dahbi M, Komaba S. Research development on sodium-ion batteries[J]. Chem. Rev., 2014, 114(23): 11636-11682.

[6] Grey C P, Tarascon J M. Sustainability and *in situ* monitoring in battery development[J]. Nat. Mater., 2017, 16(1): 45-56.

[7] Larcher D, Tarascon J M. Towards greener and more sustainable batteries for electrical energy storage[J]. Nat. Chem., 2015, 7(1): 19-29.

[8] Goodenough J B. Evolution of strategies for modern rechargeable batteries[J]. Acc. Chem. Res., 2013, 46(5):1053-1061.

[9] Goodenough J B, Kim Y. Challenges for rechargeable Li batteries[J]. Chem. Mater., 2010, 22(3): 587-603.

[10] Etacheri V, Marom R, Elazari R, Salitra G, Aurbach D. Challenges in the development of advanced Li-ion batteries: a review[J]. Energy Environ. Sci., 2011, 4(9): 3243-3262.

[11] Armand M, Tarascon J M. Building better batteries[J]. Nature, 2008, 451(7179): 652-657.

[12] Liu D Q, Shadike Z, Lin R Q, Qian K, Li H, Li K K, Wang S W, Yu Q P, Liu M, Ganapathy S, Qin X Y, Yang Q H, Wagemaker M, Kang F Y, Yang X Q, Li B H. Review of recent development of *in situ*/*operando* characterization techniques for lithium battery research[J]. Adv. Mater., 2019, 31(28): 1806620.

[13] Pecher O, Carretero-González J, Griffith K J, Grey C P. Materials' methods: NMR in battery research[J]. Chem. Mater., 2017, 29(1): 213-242.

[14] Nguyen H, Clément R J. Rechargeable batteries from the perspective of the electron spin[J]. ACS Energy Lett., 2020, 5(12): 3848-3859.

[15] Ilott A J, Mohammadi M, Schauerman C M, Ganter M J, Jerschow A. Rechargeable lithium-ion cell state of charge and defect detection by *in-situ* inside-out magnetic resonance imaging[J]. Nat. Commun., 2018, 9(1): 1776.

[16] Sathiya M, Leriche J B, Salager E, Gourier D, Tarascon J M, Vezin H. Electron paramagnetic resonance imaging for real-time monitoring of Li-ion batteries[J]. Nat. Commun., 2015, 6(1): 6276.

[17] Geng F S, Shen M, Hu B, Liu Y F, Zeng L C, Hu B W. Monitoring the evolution of local oxygen environments during $LiCoO_2$ charging via *ex situ* ^{17}O NMR[J]. Chem. Commun., 2019, 55(52): 7550-7553.

[18] Freytag A I, Pauric A D, Krachkovskiy S A, Goward G R. *In situ* magic-angle spinning ^{7}Li NMR analysis of a full electrochemical lithium-ion battery using a jelly roll cell design[J]. J. Am. Chem. Soc., 2019, 141(35): 13758-13761.

[19] Shimoda K, Murakami M, Takamatsu D, Arai H, Uchimoto Y, Ogumi Z. *In situ* NMR observation of the lithium extraction/insertion from $LiCoO_2$ cathode[J]. Electrochim. Acta, 2013, 108: 343-349.

[20] Hu B, Lou X B, Li C, Geng F S, Zhao C, Wang J Y, Shen M, Hu B W. Reversible phase transition enabled by binary Ba and Ti-based surface modification for high voltage $LiCoO_2$ cathode[J]. J. Power Sources, 2019, 438: 226954.

[21] Geng F S, Yang Q, Li C, Hu B, Zhao C, Shen M, Hu B W. Operando EPR and EPR imaging study on a $NaCrO_2$ cathode: Electronic property and structural degradation with Cr dissolution[J]. J. Phys. Chem. Lett., 2021, 12(2): 781-786.

[22] Liao Y X, Li C, Lou X B, Hu X S, Ning Y Q, Yuan F Y, Chen B, Shen M, Hu B W. Carbon-coated $Li_3V_2(PO_4)_3$

derived from metal-organic framework as cathode for lithium-ion batteries with high stability[J]. Electrochim. Acta, 2018, 271: 608-616.

[23] Yin S C, Grondey H, Strobel P, Huang H, Nazar L F. Charge ordering in lithium vanadium phosphates: electrode materials for lithium-ion batteries[J]. J. Am. Chem. Soc., 2003, 125(2): 326-327.

[24] Li C, Lou X B, Shen M, Hu X S, Yan W S, Zou Y, Tong W M, Hu B W. High-capacity cobalt-based coordination polymer nanorods and their redox chemistry triggered by delocalization of electron spins[J]. Energy Storage Mater., 2017, 7: 195-202.

[25] Li C, Yang Q, Shen M, Ma J Y, Hu B W. The electrochemical Na intercalation/extraction mechanism of ultrathin cobalt(II) terephthalate-based MOF nanosheets revealed by synchrotron X-ray absorption spectroscopy[J]. Energy Storage Mater., 2018, 14: 82-89.

[26] Li C, Hu X S, Tong W, Yan W S, Lou X B, Shen M, Hu B W. Ultrathin manganese-based metal-organic framework nanosheets: Low-cost and energy-dense lithium storage anodes with the coexistence of metal and ligand redox activities[J]. ACS Appl. Mater. Interfaces, 2017, 9 (35): 29829-19838.

[27] Li C, Lou X B, Yang Q, Zou Y M, Hu B W. Remarkable improvement in the lithium storage property of $CO_2(OH)_2$ BDC MOF by covalent stitching to graphene and the redox chemistry boosted by delocalized electron spins[J]. Chem. Eng. J., 2017, 326: 1000-1008.

[28] Li C, Shen M, Hu B, Lou X B, Zhang X, Tong W, Hu B W. High-energy nanostructured $Na_3V_2(PO_4)_2O_{1.6}F_{1.4}$ cathodes for sodium-ion batteries and a new insight into their redox chemistry[J]. J. Mater. Chem. A, 2018, 6(18): 8340-8348.

[29] Li C, Shen M, Lou X B, Hu B W. Unraveling the redox couples of V-III/V-IV mixed-valent $Na_3V_2(PO_4)_2O_{1.6}F_{1.4}$ cathode by parallel-mode EPR and *in situ*/*ex situ* NMR [J]. J. Phys. Chem. C, 2018, 122(48): 27224-27232.

[30] Park Y U, Seo D H, Kim B, Hong K P, Kim H, Lee S, Shakoor R A, Miyasaka K, Tarascon J M, Kang K. Tailoring a fluorophosphate as a novel 4 V cathode for lithium-ion batteries[J]. Sci. Rep., 2012, 2: 704.

[31] Qiu Q, Li C, Liu H, Liao Y X, Zhao C, Geng F S, Shen M, Li J X, Tong W, Hu B W. NMR evidence for the multi-electron reaction mechanism of $Na_3V_2(PO_4)_3$ cathode and the impact of polyanion site substitution[J]. J. Phys. Chem. C, 2021, 125(28): 15200-15209.

[32] Li C, Zhao C, Hu B, Tong W, Shen M, Hu B W. Unraveling the critical role of Ti substitution in P2-$Na_xLi_yMn_{1-y}O_2$ cathodes for highly reversible oxygen redox chemistry[J]. Chem. Mater., 2020, 32(3): 1054-1063.

[33] Zhao C, Li C, Yang Q, Qiu Q, Tong W, Zheng S, Ma J Y, Shen M, Hu B W. Anionic redox reaction in Na-deficient layered oxide cathodes: Role of Sn/Zr substituents and in-depth local structural transformation revealed by solid-state NMR[J]. Energy Storage Mater., 2021, 39: 60-69.

[34] Geng F S, Hu B, Li C, Zhao C, Lafon O, Trébosc J, Amoureux J P, Shen M, Hu B W. Anionic redox reactions and structural degradation in a cation-disordered rock-salt $Li_{1.2}Ti_{0.4}Mn_{0.4}O_2$ cathode material revealed by solid-state NMR and EPR[J]. J. Mater. Chem. A, 2020, 8(32): 16515-16526.

[35] Li C, Shen M, Hu B W. Solid-state NMR and EPR methods for metal ion battery research[J]. Acta Phys.-Chim. Sin., 2020, 36(4): UNSP 1902019.

[36] Liu Y F, Zeng L C, Xu C C, Geng F S, Shen M, Yuan Q H, Hu B W. Optimizing the Ueff value for DFT+U calculation of paramagnetic solid-state NMR shifts by double Fermi-contact-shift verification[J]. Chem. Phys. Lett., 2019, 736: 136779.

[37] Pigliapochi R, Pell A J, Seymour I D, Grey C P, Ceresoli D, Kaupp M. DFT investigation of the effect of spin-orbit coupling on the NMR shifts in paramagnetic solids[J]. Phys. Rev. B, 2017, 95: 054412

[38] Hrobárik P, Reviakine R, Arbuznikov A V, Malkina O L, Malkin V G, Köhler F H, Kaupp M. Density functional calculations of NMR shielding tensors for paramagnetic systems with arbitrary spin multiplicity: Validation on 3d metallocenes[J]. J. Chem. Phys., 2007, 126: 024107.

[39] Pigliapochi R, Seymour I D, Merlet C, Pell A J, Murphy D T, Schmid S, Grey C P. Structural characterization of the Li-ion battery cathode materials $LiTi_xMn_{2-x}O_4$ ($0.2 \leqslant x \leqslant 1.5$): A combined experimental ^{7}Li NMR and first-principles study[J]. Chem. Mater., 2018, 30(3): 817-829.

[40] Middlemiss D S, Ilott A J, Clément R l J, Strobridge F C, Grey C P. Density functional theory-based bond pathway decompositions of hyperfine shifts: Equipping solid-state NMR to characterize atomic environments in paramagnetic materials[J]. Chem. Mater., 2013, 25: 1723-1734.

[41] Castets A, Carlier D, Zhang Y, Boucher F, Ménétrier M. A DFT-based analysis of the NMR fermi contact shifts in tavoritelike $LiMPO_4 \cdot OH$ and $MPO_4 \cdot H_2O$ (M = Fe, Mn, V) [J]. J. Phys. Chem. C, 2012, 116: 18002-16014.

金属离子电池中的磁共振：从核磁共振(NMR)到电子顺磁共振(EPR)

胡炳文*,李 超,耿福山,沈 明

(华东师范大学物理与电子科学学院,上海市磁共振重点实验室,上海 200062)

摘要: 金属离子电池改变了我们的日常生活。金属离子电池里的电极材料研究是提高电池性能的关键。因此,深刻理解电极材料的结构-性能关系,有助于提高材料的能量密度和功率密度。磁共振,包括核磁共振(NMR)和电子顺磁共振(EPR),在过去的三十年中不断得到改进,并逐渐成为研究电极材料结构性能关系的重要技术之一。本文总结了我们课题组在几种有趣的电极材料上的磁共振研究进展,阐释了 NMR 和 EPR 在电极材料研究中的重要作用。本文将有助于把握磁共振技术对电池研究的重要价值,促进磁共振技术的进一步发展。

关键词: 固态核磁共振;电子顺磁共振;电池;正极材料